Available online at www.sciencedirect.com

SciVerse ScienceDirect

Geochimica et Cosmochimica Acta 109 (2013) 254–267

Geochimica et Cosmochimica Acta

www.elsevier.com/locate/gca

Climatic and diagenetic signals in the stable isotope geochemistry of dolomitic paleosols spanning the Paleocene–Eocene boundary

Justin H. VanDeVelde [a,*], Gabriel J. Bowen [a,1], Benjamin H. Passey [b], Brenda B. Bowen [a,1]

[a] Department of Earth, Atmospheric and Planetary Sciences, Purdue University, West Lafayette, IN 47907, USA
[b] Department of Earth and Planetary Sciences, Johns Hopkins University, 3400 North Charles Street, Baltimore, MD 21218, USA

Received 28 May 2012; accepted in revised form 1 February 2013; Available online 15 February 2013

Abstract

The precipitation of primary dolomite in soil is rare and controversial, and its occurrence indicates highly unusual geochemical and climatic conditions. We utilize isotopic and petrographic techniques, including clumped isotope thermometry, to evaluate diagenetic alteration and preservation of primary climatic signal in dolomitic paleosol nodules from a section spanning the Paleocene–Eocene boundary in central Utah. Isotopic measurements differentiate samples into groups that may be interpreted in terms of alteration; however moderate burial depths and extreme warmth during the interval of soil formation make it difficult to reach definitive conclusions from isotope values alone. With the addition of petrographic analysis, including cathodoluminescence and scanning electron microscopy, we are able to identify textural differences between samples suggesting differing amounts of recrystallization. We conclude that while some nodules have experienced significant diagenetic alteration the original nodule mineralogy is dolomite, and the majority of sampled nodules retain a primary paleoclimate signal. Early Paleogene temperatures recorded at this site are considerably warmer than those suggested for the continental interior from alternate proxies, a result that may be partially the result of the clumped isotope temperatures recording warm season soil temperatures, rather than mean annual air temperature. Soil water isotopic composition is suggestive of heightened aridity, particularly through the Paleocene–Eocene Thermal Maximum (PETM).

1. INTRODUCTION

Paleoclimate reconstructions indicate that the early Eocene was the warmest interval on Earth within the past 65 million years. Recently developed marine paleoclimate records have produced variable estimates of early Eocene warmth, with reconstructed mid- and high latitude temperatures >30 °C (Zachos et al., 2006; Bijl et al., 2009) contrasting with cooler temperatures estimated for the subtropics (Keating-Bitonti et al., 2011). Understanding the mechanisms responsible for early Eocene warmth has been rendered more difficult by the spatial distribution of most proxy localities within both the marine and continental realm. Sites from the continental interior have generally indicated very warm mean annual and particularly winter temperatures, and the failure of modern climate models to reproduce these conditions accurately has come to be known as the "equable climate" problem (Sloan, 1994; Huber and Caballero, 2011). Resolution of this problem depends upon establishing new climate proxy localities for the early Eocene from continental interiors.

* Corresponding author. Present address: School of Geography, Earth and Environmental Sciences, Plymouth University, Drake Circus, Plymouth, Devon PL4 8AA, UK
E-mail address: justin.vandevelde@plymouth.ac.uk (J.H. VanDeVelde).
[1] Present address: Department of Geology and Geophysics, University of Utah, Salt Lake City, UT 84112, USA.

0016-7037/$ - see front matter © 2013 Elsevier Ltd. All rights reserved.
http://dx.doi.org/10.1016/j.gca.2013.02.005

Additionally, the interval leading up to and immediately following the Paleocene–Eocene boundary is marked by profound, abrupt and temporary shifts in the global climate and carbon cycle. The largest and best-studied of these excursions, the Paleocene–Eocene Thermal Maximum (PETM), is characterized by a global temperature increase of 5–8 °C and an associated release of thousands of Pg of carbon into the atmosphere (McInerney and Wing, 2011), producing a prominent negative carbon isotope excursion (CIE) in marine and continental sediments. In continental records, significant variability occurs in the magnitude of the CIE between sites and among different substrates, reflecting the interaction between a global carbon pulse and regional environmental factors, and complicating interpretations of the CIE as a constraint on the source and mechanisms of carbon cycle perturbation during the event. A number of mechanisms have been suggested to explain these regional variations, including regional hydroclimatology (Bowen et al., 2004), or differential responses in plant physiology (Schouten et al., 2007) and/or community change (Smith et al., 2007; Diefendorf et al., 2010). In order to test these hypotheses and improve our understanding of regional continental climatic impacts of the PETM there is a need for new terrestrial climate records in geographically separate regions, and particularly along latitudinal gradients.

1.1. The Axhandle Canyon PETM section

A new continental PETM section was identified by Bowen and Bowen (2008) based on preservation of a robust CIE in pedogenic carbonate nodules from a section of the upper North Horn Formation in the Axhandle paleo-basin of central Utah (Fig. 1A). Previously existing age constraints for this section include paleomagnetic stratigraphy (Talling et al., 1994), and early Eocene vertebrate remains recovered in an adjacent canyon from the Flagstaff Formation (Rich and Collinson, 1973), a unit of lacustrine carbonates that overlies the North Horn Formation in Axhandle Canyon and elsewhere in the region. These age constraints indicate that any negative CIE found in this section within ~100 m of the Flagstaff-North Horn contact is likely to represent the PETM.

The North Horn Formation in this area consists of several hundred meters of pedogenically modified clastic sediments deposited by fluvial systems draining the eastern flanks of the Sevier highlands (Lawton and Trexler, 1991). Evidence of pedogenesis in the Axhandle Canyon section includes variegated coloration, root traces, burrows, depletion channels, and occurrences of carbonate as discrete nodules. As we report here, these nodules are preserved primarily as micritic dolomite. Low-magnesium calcite is the dominant authigenic carbonate mineralogy in both modern and ancient soils, and the presence of dolomite in paleosols is usually considered a product of post-burial diagenesis (Sheldon and Tabor, 2009). However, dolomite has been found precipitating in modern soils under arid conditions (Kohut et al., 1995; Capo et al., 2000), while ancient soils with nodular dolomite considered pedogenic in origin have been documented from the Permian (Kessler et al., 2001; Kearsey et al., 2012) and Pliocene (He et al., 2012). Formation of pedogenic dolomite is thought to be due to high Mg^{2+} activity in soil water, coupled with extreme soil evapotranspiration (Sheldon

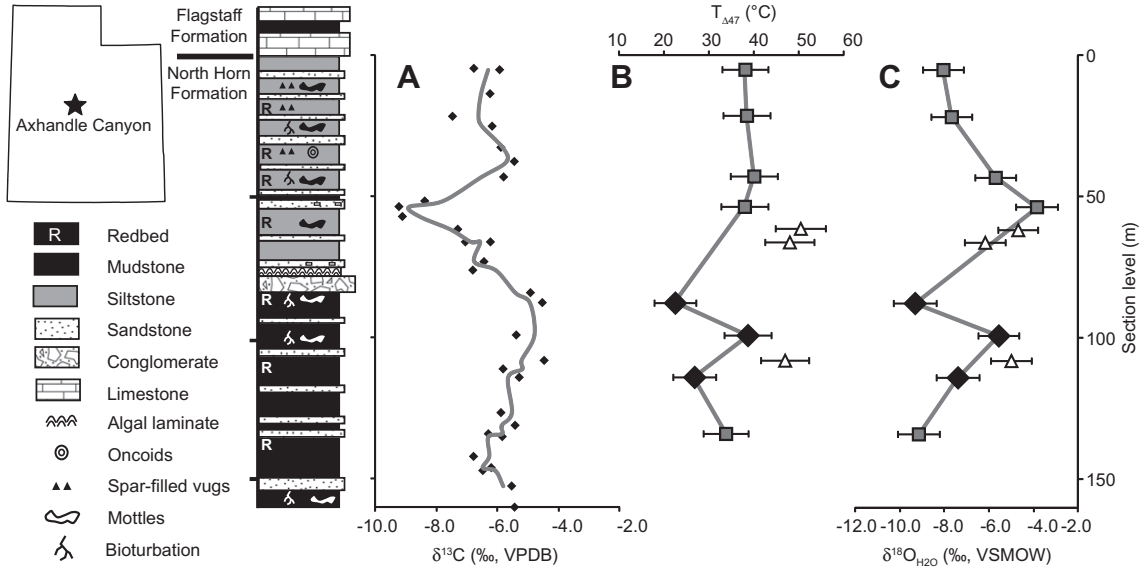

Fig. 1. Stable isotope and lithostratigraphy of Axhandle canyon study section. Inset – line map of Utah, with location of Axhandle Canyon study section highlighted. Panel A – paleosol carbonate $\delta^{13}C$ record of Bowen and Bowen (2008), with curve showing 3-point running average values. Panel B – clumped isotope-derived temperatures from nodule carbonate, calculated using the calibration of Guo et al. (2009). Panel C – oxygen isotope composition of water in equilibrium with carbonate micrite, based on measured $\delta^{18}O_{CO_3}$, the Δ_{47} temperature estimates, and the equation of Vasconcelos et al. (2005). For panels B and C: black diamonds – category 1 nodules; gray squares – category 2; white triangles – category 3, with tie points connecting the two least altered sample categories (1 and 2). Error bars represent 1σ propagated uncertainty.

and Tabor, 2009). The Axhandle section therefore provides a unique opportunity to examine both an extremely rare geochemical phenomena, as well as to better understand early Paleogene climate conditions.

The negative carbon isotope excursion in the Axhandle section is ~2‰ smaller than that found in PETM soil carbonates of the Bighorn Basin of northern Wyoming, while the ~2‰ positive excursion in oxygen isotope values is roughly twice that observed in the Bighorn Basin (Bowen et al., 2001). Bowen and Bowen (2008) hypothesized that the greater magnitude of the Axhandle oxygen isotope excursion reflects greater evaporative enrichment of soil water in an arid climate. However, interpretation of $\delta^{18}O$ values from soil carbonate in terms of hydroclimatologic change is complicated by the composite nature of this signal, which is controlled by both the composition of soil water from which the nodules were precipitating and the soil temperature during precipitation.

1.2. Clumped isotope paleothermometry: theory and practice

The carbonate "clumped isotope" paleothermometer has the potential to disentangle the effects of temperature and water composition on carbonate oxygen isotopes. This proxy is based on the tendency of ^{13}C and ^{18}O to associate or "clump" in the carbonate crystal lattice. A certain amount of random clumping occurs and can be predicted by probability theory given knowledge of the relative abundances of each isotope. However, divergence from this random association occurs because 'clumped' species have lower free energies than 'unclumped' species, and this divergence is temperature dependent (Schauble et al., 2006; Ghosh et al., 2006). Simultaneous measurement of the mass 44, 45, 46 and 47 isotopologues allows for the calculation of this divergence, hereafter referred to as Δ_{47} and expressed in units of per mille (‰). Both experimental and theoretical relationships have been developed that relate Δ_{47} to the temperature of mineral growth (Ghosh et al., 2006; Schauble et al., 2006; Guo et al., 2009). In addition, when this clumped isotope-based temperature estimate is combined with the simultaneously measured $\delta^{18}O$ values of carbonate, it is possible to calculate the $\delta^{18}O$ of coexisting water using an appropriate carbonate-water oxygen isotope thermometry equation (e.g., Kim and O'Neil, 1997; Vasconcelos et al., 2005).

In order to interpret isotope analyses in terms of primary climatic signals we must consider the potential of diagenesis to partially or completely reset the isotopic system to burial values. Unlike the carbon and oxygen isotope systems, the clumped isotope system is susceptible to resetting during closed-system recrystallization. That is, ^{13}C–^{18}O bonds within the mineral structure can be reordered during minor recrystallization, and such recrystallization can occur without major exchanges with burial fluids that would be necessary to significantly affect $\delta^{13}C$ or $\delta^{18}O$ values (Dennis and Schrag, 2010).

Here, we report Δ_{47}-derived temperature estimates from dolomitic North Horn paleosol carbonates, and undertake a rigorous examination of the section using both isotopic and petrographic techniques, in order to assess the presence and extent of diagenetic influences on the mineralogy and Δ_{47} values for these samples. Our objective is to test whether these dolomitic nodules are the product of primary, near-surface processes, and if they can provide useful insight into the paleoclimate of this region.

2. METHODS

2.1. Sample selection and isotopic analyses

The carbonate nodules for clumped isotope analysis were selected from the sample set of Bowen and Bowen (2008), which included 59 stratigraphic levels, with at least 2–3 nodules from each level, sampled at a minimum of 30 cm below the upper surface of each paleosol. From this collection, we selected a total of 11 individual nodules, each from a separate paleosol, attempting to capture the range of stratigraphic and isotopic variation within the study section, targeting stratigraphic levels that displayed a minimum of isotopic variation between individual nodules. Nodules were first slabbed, polished and examined under magnification. Cubes (~5 mm on a side) were then cut from the interior of each nodule using a lapidary saw, evaluated under magnification to avoid sampling sparry carbonate cement, and then ground using mortar and pestle.

Aliquots (~10 mg) of powder from each sample were analyzed at the Johns Hopkins University Stable Isotope Lab after the methods of Ghosh et al. (2006) as modified by Passey et al. (2010). Each aliquot was reacted at 90 °C with 100% phosphoric acid, with the resultant CO_2 being cryogenically purified before analysis on a Thermo MAT 253 mass spectrometer. Mass ratios (R), normalized to the mass 44 signal, were measured for all stable CO_2 isotopologues, and Δ_{47} was calculated as:

$$\Delta_{47} = \left[\left(\frac{R^{47}}{R^{47*}} - 1\right) - \left(\frac{R^{46}}{R^{46*}} - 1\right) - \left(\frac{R^{45}}{R^{45*}} - 1\right)\right] \times 1000,$$

where R^{x*} is the ratio for a sample of determined bulk isotopic composition, but with stochastic isotopologue speciation (Affek and Eiler, 2006). Measurements of Δ_{47} are normalized relative to CO_2 gas aliquots heated to 1000 °C to achieve stochastic abundances of isotopologues (Huntington et al., 2009), and relative to CO_2 gas equilibrated with water at 27 or 30 °C (Wang et al., 2004; Dennis et al., 2011), and an acid temperature correction of 0.081‰ was applied to normalize Δ_{47} values to the scale for 25 °C phosphoric acid reactions (Passey et al., 2010). During the course of the study an internal Carrara marble standard (UU Carrara) was analyzed 15 times with a mean Δ_{47} value of 0.354‰ and a precision of 0.009‰; another internal standard (102-GC-AZ01) analyzed 16 times yielded $\Delta_{47} = 0.646 \pm 0.014$‰. Each unknown was analyzed twice, and the precision for unknowns was estimated as the mean difference between each pair of analyses (0.015‰). The standard error of the mean is thus 0.010‰ (0.015‰/$\sqrt{2}$).

Temperature was calculated from the measured Δ_{47} values using the theoretical dolomite calibration of Guo et al. (2009), or the experimental calcite calibration of Ghosh et al. (2006). Synthetic dolomites grown at low temperatures (Ferry et al., 2011) overlap the theoretical dolomite

calibration. We use the dolomite calibration for all paleosol samples, as for most samples the calibrations produce temperature estimates that differ by less than the analytical uncertainty. For those samples where the calibrations produce significantly different temperatures, our mineralogic analyses indicate the carbonate mineralogy is pure dolomite. Our estimated temperature uncertainties of 3–6 °C derive from the 0.010‰ analytical error and an estimated error of 0.0028‰ for the acid temperature correction (Passey et al., 2010), both propagated through the temperature calibration equations. Values of $\delta^{18}O_{H_2O}$ are then calculated from T and $\delta^{18}O_{CO_3}$ using the calibration of Vasconcelos et al. (2005) for dolomite, and Kim and O'Neil (1997) for calcite. We use the dolomite fractionation for paleosol samples, and the calcite fractionation for our spar sample.

None of the Axhandle nodules had spar present in sufficient, physically separable quantities for Δ_{47} measurement. To estimate the composition of regional burial cements, measurements were made of equant fracture-filling spar crystals recovered from the upper Flagstaff Formation, in the vicinity of Musinia Peak, ~20 km southeast of the Axhandle locality. The Flagstaff Fm. is a sequence of lacustrine authigenic carbonates that locally interfingers with the North Horn Fm. and directly overlies it in the Axhandle section (Talling et al. 1994; Bowen and Bowen, 2008), and was buried to a similar maximum depth (Hintze, 1988); therefore late-stage burial diagenetic materials are likely to record comparable conditions. In order to provide a basis for comparison of the Flagstaff spar with that present in the North Horn samples, microsamples of spar for bulk isotope analysis ($\delta^{13}C$, $\delta^{18}O$) were obtained from two nodules (NH060124 and NH060128). Additionally, comparison between North Horn paleosol nodules and lacustrine carbonates of the Flagstaff Formation was facilitated by bulk isotope analysis of micrites ($n = 16$) sampled from ~15 meters above the top of the measured Axehandle Canyon section. All microsamples were obtained from slabbed and polished faces using a dental drill under a binocular microscope. These microsamples were reacted with orthophosphoric acid at 70 °C, with the resultant CO_2 being chromatographically purified on a GasBench and analyzed utilizing a ThermoFinnigan Delta V mass spectrometer at the Purdue Stable Isotope Lab. Values were standardized to the VPDB reference scale using an in-house Carrera Marble standard, with an analytical precision of 0.1‰ for both $\delta^{13}C$ and $\delta^{18}O$ (1σ) based on replicate analyses of an independent check standard.

2.2. Petrographic analysis

Polished thin sections were produced from each nodule measured for Δ_{47} values and examined utilizing transmitted light and cathodoluminescence microscopy to characterize their primary and diagenetic fabrics. Constituents of each nodule were quantitatively determined through point counting of 500 regularly spaced points on sections stained with alizarin red. Constituents were categorized as micritic carbonate, sparry carbonate cement, or siliciclastic grains; no detrital carbonate, identified as macroscopic inclusions with substantially different color or textural differences from the nodular matrix, was observed in any nodule. Each nodule was described qualitatively under cathodoluminescence (CL). Luminescence intensity is controlled by minor chemical constituents, primarily Mn^{2+}, which causes an orange luminescence, and Fe^{2+}, which quenches luminescence (Hemming et al. 1989). Presence of these elements is related to redox conditions, with the result being that carbonates precipitated under differing chemical conditions can be identified (Machel and Burton, 1991; Solomon and Walkden, 1985).

Polished thin sections were imaged with an FEI Quanta 3D FEG scanning electron microscope (FEI Company, Hillsboro, OR), using the low vacuum secondary electron detector (LVSED) at 0.75 T. Parameters were 20 kV, spot 6.0, and working distance of ~10 mm. X-ray analysis (EDX) was done with an Oxford INCA Xstream-2 with Xmax80 silicon drift detector (Oxford Instruments, Peabody, MA) using the above parameters and 50 μm objective aperture. Spectra were collected for 60 s.

2.3. Mineralogic analyses

X-ray diffraction (XRD) was performed on those nodules analyzed for Δ_{47} which had sufficient powdered material remaining after Δ_{47} analysis ($n = 6$). Self-supporting powder mounts were prepared using an aluminum sample holder. Diffraction patterns were obtained using a PANalytical X'Pert PRO MPD X-ray diffraction system (PANalytical, Almelo, The Netherlands) equipped with a PW3050/60 θ–θ goniometer and a Co-target X-ray tube operated at 40 keV and 35 mA. Incident beam optics consisted of a Fe beta filter, 0.04 rad Soller slit, a programmable divergence slit, and a beam mask set to illuminate a 10 × 10 mm sample area. A fixed, 1° antiscatter slit was used at diffraction angles <12° 2θ. The diffracted beam optics consisted of a programmable diffracted beam antiscatter slit, a 0.04 rad Soller slit, and a PW3015/20 X'Celerator detector configured for an active length of 2.12° 2θ. Samples were scanned from 2° to 40° 2θ at 0.03° steps. Mineralogical composition of each sample was quantified using the X'Pert High Score Plus software package, and was converted to a fixed 1° divergence slit prior to phase analysis and plotting.

Slabbed faces of nodules from Axhandle Canyon were analyzed in the laboratory using a Fieldspec 3 Analytical Spectral Device (ASD), with a visible/near-infrared-shortwave infrared spectral range from 350 to 2500 nm and wavelength sampling ranging from 3–10 nm. The ASD contact probe is self-illuminated and has a 1 cm diameter spot size. Subsequent spectral analysis focused on the shortwave infrared ~2300 nm carbonate absorption feature (Gaffey, 1986) in order to distinguish calcite (~2340 nm) from dolomite (~2320 nm).

3. RESULTS

3.1. Petrography

Petrographic results are summarized along with the isotopic data in Table 1. In order to guide interpretation of our

Table 1
Summary of isotopic and petrographic analyses.

Sample ID	Meter level	Petrographic category[a]	$\delta^{13}C$ (VPDB)	$\delta^{18}O$ (VPDB)	Δ_{47} ‰, Ghosh scale[b]	Δ_{47} ‰, Equil. scale[c]	T_{47} (°C)[d]	$\delta^{18}O_{H_2O}$[e]	% Micrite	% Spar	% Siliciclastic	Carbonate absorption minimum[f] (nm)	Calcite/ dolomite ratio[g]	Micrite Mg/Ca[h]
FF-Spar		Spar	−8	−14.9	0.546	0.590	50 ± 3	−8	0	100	0	–	–	–
NH060107	136.0	2	−6.6	−10.3	0.591	0.636	34 ± 5	−9	70	5.6	24.4	2330	–	–
NH060110	116.0	1	−5.5	−7.2	0.610	0.660	27 ± 5	−7	95	0	5	2322	0	0.91 ± .03
NH060112	110.0	3	−4.8	−8.5	0.558	0.604	47 ± 5	−5	60	10	30	2334	–	–
NH060113	101.0	1	−5	−7.6	0.579	0.624	39 ±5	−6	90	0	10	2326	0	0.84 ± .06
NH060114	89.5	1	−4.8	−8.2	0.623	0.674	22 ± 5	−9	91.3	0	8.7	2325	0	0.84 ± .08
NH060119	68.0	3	−6.3	−9.8	0.556	0.601	48 ± 6	−6	55	20	25	2336	0.96	0.72 ± .01
NH060120	63.5	3	−8.6	−8.7	0.550	0.595	50 ± 6	−5	78.2	7.4	14.4	2336	0.5	0.82 ± .08
NH060122	55.5	2	−9.4	−5.8	0.580	0.627	38 ± 5	−4	75.4	6.6	18	2322	–	0.83 ± .06
NH060124	45.0	2	−6.7	−8	0.575	0.623	40 ± 5	−6	77	14.2	8.8	2330	–	0.54 ± .06
NH060128	23.5	2	−7.7	−9.7	0.579	0.626	38 ± 5	−8	81.3	15	3.7	2336	0.51	0.28 ± .13
NH060130	7.0	2	−6.5	−10	0.580	0.630	38 ± 5	−8	80	5	15	2336	0.61	0.14 ± .04

Note: Standard error of the mean (SEM) for $\delta^{13}C$, $\delta^{18}O$, Δ_{47} (Ghosh), and Δ_{47} (Equilibrium scale) are 0.02‰, 0.04‰, 0.010‰, and 0.013‰, respectively.

[a] Based on point counts and CL microscopy.

[b] Δ_{47} Values relative to the 'Ghosh' scale (Ghosh et al., 2006), as described in Huntington et al. (2009), using a canonical heated gas intercept of 0.8453‰, and normalized to 25 °C reactions by addition of a 0.081‰ temperature correction factor for 90 °C reactions (Passey et al., 2010).

[c] Δ_{47} Values reported on an 'equilibrium carbon dioxide scale' described in Dennis et al. (2011).

[d] *T* for FF09011 calculated using experimental calcite calibration of Ghosh et al. (2006); all others using theoretical dolomite calibration of Guo et al. (2009); error calculated by standard propagation (root sum of squares) of error in Δ_{47} (0.010‰) and error in acid temperature correction factor (0.0028‰).

[e] FF09011 Kim and O'Neil (1997); all others (Vasconcelos et al., 2005). Standard error is 1‰.

[f] Minimum wavelength of 2300 nm carbonate absorption feature from IR spectroscopy.

[g] Semi-quantitative estimate from XRD.

[h] Average of all micrite EDX measurements from each sample.

petrographic analyses, we used them to assign each nodule according to a 3-tier classification scheme (Fig. 2), with category 1 samples exhibiting little or no features suggestive of post-burial alteration, category 2 samples exhibiting moderate evidence of alteration, and category 3 being the most altered samples. Under CL microscopy (Fig. 3), category 1 nodules exhibit uniform degrees of orange-red luminescence throughout, though the luminescence intensity is variable between nodules. All category 2 assignments were based on the presence of spar filling nodule pores. Cements typically exhibited luminescence intensities very similar to that of the micritic matrix, and tended to occur as narrow, linear pore or crack-fills. Two of the category 3 samples had patterns of highly variable luminescence behavior that were spatially intermixed. We did not observe any association of luminescence patterns with other petrographic features such as pores or detrital grains, but regions of varying luminescence were more generally scattered throughout the matrix. In transmitted light these regions were difficult to identify as either micritic or sparry carbonate, with large crystallites throughout (Fig. 4). In contrast, sample NH060120 did not contain these large, intermixed crystallites, but exhibited multiple phases of luminescence in the micritic matrix. These phases were spatially distinct within the sample, but were present within the interior of the nodule and therefore could not be identified as an alteration rind, and the sample was identified as category 3. Additionally, the pore-filling spar in all category 3 samples exhibits multiple, distinct luminescent phases, although it was not possible to develop a consistent cement stratigraphy for multiple nodules.

Point counts indicate that the primary constituent of the nodules is fine-grained micrite, composing 60–95% of each thin section. Detrital siliciclastic grains, largely quartz, are present in quantities ranging from 3.7% to 30%. Cement occurs as pore-filling, coarse mosaic spar in many nodules, comprising 0–15% of the points counted. Spar microsamples from North Horn Fm. carbonate nodules (Table 2) exhibit isotopic values that are more similar to those of the micritic carbonate in nodules from which they were obtained than to the values of the Flagstaff Fm. spar. Although $\delta^{13}C$ differs by as much as 1.4‰ between micrite and spar from the same nodule, $\delta^{18}O$ values for all microsamples are within 1‰ of the coexisting nodule micrite. In contrast, the average $\delta^{18}O$ value for the North Horn Fm. spars was 5.3‰ higher than that of the Flagstaff Fm. sample. Lacustrine Flagstaff micrites from the top of the Axehandle section exhibit $\delta^{18}O$ values (-9.2 ± 1.3‰ 1σ) similar to nodule micrites (avg. $= -8.7 \pm 1.0$‰ 1σ). Lacustrine $\delta^{13}C$ values (-4.4 ± 0.9‰ 1σ) are distinct from nodule values (-6.3 ± 1.1‰ 1σ, $p << 0.001$).

3.1.1. Isotopic analyses

A summary of isotopic results is provided in Table 1. Full details of clumped isotope analyses, including standards measured over the period of sample analysis are listed in a Supplementary Table. Δ_{47} values for all samples ranged from 0.546‰ to 0.623‰, with an average difference between replicate measurements of 0.015‰ (maximum = 0.028‰, minimum = 0.003‰); utilizing the theoretical dolomite temperature calibration for dolomite of Guo et al. these values translate to temperatures of 22–50 °C. As some samples exhibit mixed dolomite and calcite mineralogy, temperatures were also calculated utilizing the empirical calibration of Ghosh et al. (2006). For nearly all samples, this results in temperature estimates within 2 °C of the Guo calibration. Temperature estimates from samples NH060110 and NH060114 differ by up to 8 °C based on the calibration used, but mineralogic analyses show that both samples are purely dolomitic. The $\delta^{18}O$ values of water in equilibrium with the precipitating dolomite or calcite range from −9‰ to −4‰ VSMOW. The highest temperature and lowest $\delta^{18}O_{H_2O}$ value are both from the calcite spar sample from the Flagstaff Limestone. For the nodule samples, higher temperatures are moderately associated with higher $\delta^{18}O_{H_2O}$ values ($R^2 = 0.46$).

Nodule samples exhibit considerable stratigraphic variation in precipitation temperature (Fig. 1B). Two prominent maxima occur at the 68 and 110 m levels, separated by the lowest measured temperature at 89.5 m, although these maxima occur in samples regarded as most likely to be diagenetically altered (see Section 4.2). Values are less variable at the top of the section, with the uppermost four nodules giving an average temperature of 39 °C. Values of

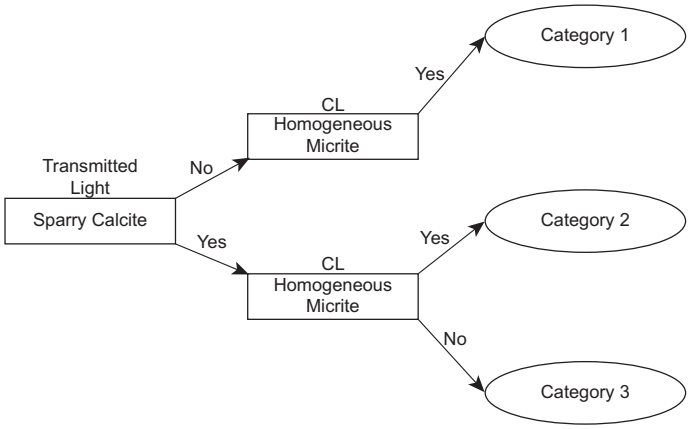

Fig. 2. Conceptual flowchart for petrographic categorization of carbonate nodules.

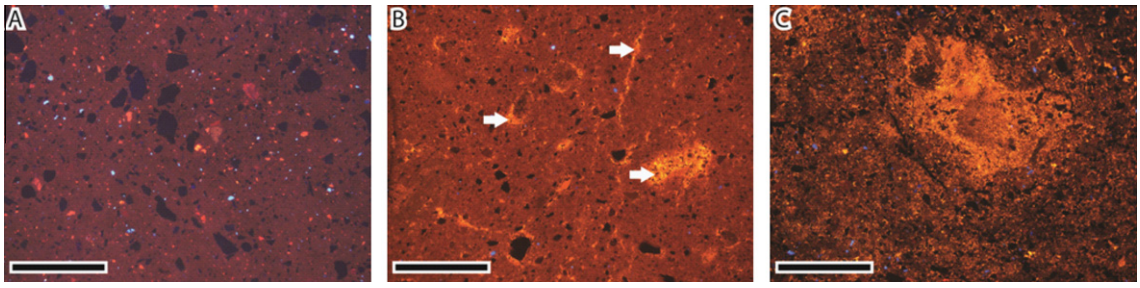

Fig. 3. CL photomicrographs of representative nodules. (A) Category 1 ($n = 3$), exhibiting uniform dull luminescence, with no evidence of cement fill or matrix recrystallization. (B) Category 2 ($n = 5$), with uniform matrix luminescence and pore-filling calcite spar (arrows). (C) Category 3 ($n = 3$) with ubiquitous, intimately mixed variations in luminescence. Scale bars in all images are 1 mm. Micrographs images have been post-processed to enhance contrast for identifying within-sample variance in luminescence.

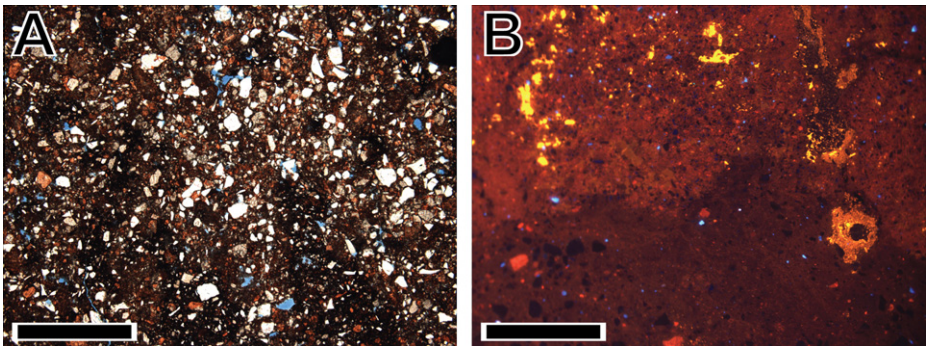

Fig. 4. CL photomicrographs of 2 category 3 nodules. (A) Sample NH060112, a category 3 sample, under plane-polarized light, showing extensive heterogeneity in micrite texture and development of large calcite crystals suggestive of matrix recrystallization. (B) Sample NH060120, also category 3, in cathodoluminescence. Note multiple intensities of micrite luminescence, as well as extensive pore-filling spar. Scale bars 1 mm. Micrographs have been post-processed to enhance contrast of luminescence features.

Table 2
Bulk isotopic values of spar microsamples obtained from North Horn Fm. nodules. Sample IDs are those of the nodule from which they were obtained (see Table 1).

Nodule Sample ID	$\delta^{13}C_{CO_3}$ (‰, VPDB)	$\delta^{18}O_{CO_3}$ (‰, VPDB)
NH060124-A	−6.9	−9
NH060128-A	−9.0	−10.2
NH060128-B	−8.0	−9.6
NH060128-C	−8.3	−9.6

$\delta^{18}O_{H_2O}$ exhibit similar stratigraphic trends to Δ_{47} (Fig. 1C), though local maxima occur at slightly (~5 m) different stratigraphic levels.

3.2. Mineralogy

Results of IR spectroscopy, XRD and SEM/EDX analyses are summarized in Table 1. XRD analysis shows that the mineral constituents of all nodules are dolomite, quartz, calcite and minor kaolinite. Calcite content ranges from 0% to 30%, whereas quartz is 11–38% of the mineral content. Calcite content generally increases up-section, but is more closely related to the established petrographic categories. In those nodules identified as category 1, which lack sparry cements, XRD identified no calcite component, and all carbonate present occurs as dolomite. In SEM imagery, this carbonate occurs as 1–10 μm crystals exhibiting interlocking growth patterns (Fig. 5A). EDX analyses show that this microcrystalline carbonate is exclusively dolomite, with near-stoichiometric Mg/Ca ratios. XRD results from category 2 and 3 samples indicate the presence of both calcite and dolomite. Where coarsely crystalline carbonate spar is present in category 2 and 3 samples, EDX analysis shows that it is low-magnesium calcite (Fig. 5B).

IR spectroscopy of all nodules from the section of Bowen and Bowen (2008) on the north wall of Axhandle Canyon, from which the samples for clumped isotope analysis were culled, indicates that dolomite is present in nodules throughout the section (Fig. 6). Absorption minima of the 2300 nm carbonate feature range from 2320 nm indicating pure dolomite, to 2340 nm characteristic of calcite. Spectra are a mix of intermediate values at the bottom of the section, decreasing up-section to mostly dolomite signatures around the 80 m level, returning to intermediate values above 100 m and remaining so for the rest of the section. These results generally agree with the more precise mineralogy determined from XRD, but comparison shows that nodules with an absorption minimum at 2340 nm can still be 50% or more dolomite. The spectroscopic results are therefore better used in a qualitative sense to identify nod-

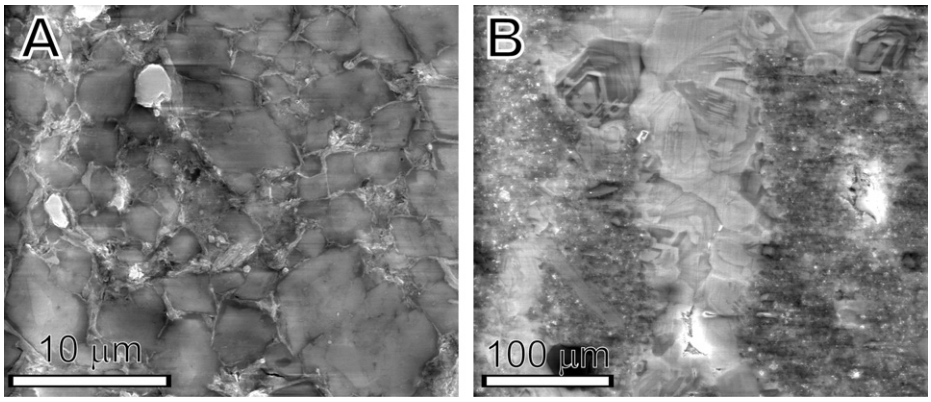

Fig. 5. SEM images from two dolomitic paleosol nodules. (A) NH060113 at 10,000×, showing microcrystalline micrite composed of 1–10 μm carbonate crystals with interlocking, rhombic growth habits. EDX shows these crystals to be dolomitic. (B) NH060128 at 800×, showing a pore-filling vein of coarsely crystalline spar, with distinct separation from the microcrystalline groundmass. EDX identifies the spar as low-magnesium calcite.

ules with and without calcite, rather than as a basis for establishing relative mineral contents.

4. DISCUSSION

4.1. Isotopic screening for diagenesis

Our clumped isotope data provide temperatures that, if interpreted as a primary climatic signal, indicate very high and variable temperatures during the Early Paleogene in this region of the North American interior. In previous studies, much consideration has been given to whether or not a given Δ_{47} measurement records a plausible temperature for the conditions of original precipitation. In biogenic samples, e.g. dinosaur tooth enamel (Eagle et al., 2011) or mollusk shells (Huntington et al., 2010, 2011), where a strong physiological control on maximum temperature is expected, this is a reasonable criteria for rejecting a measurement, even from a sample that otherwise shows no evidence of diagenetic alteration. However, we suggest that for the Axhandle Canyon nodules, formed in an arid environment (Bowen and Bowen, 2008) during one of the warmest intervals of the previous 60 million years (Zachos et al., 2001), temperature alone may present an overly restrictive criteria for evaluating Δ_{47} measurements. Passey et al. (2010) demonstrated that in mid-latitude sites with significant seasonality of temperature, Δ_{47} measurements correlate most closely with mean warm season temperatures, rather than annual temperature. The Axhandle locality's Early Paleogene latitude of approximately 40°N (Talling et al., 1994) raises the possibility that temperatures during carbonate formation were considerably warmer than mean annual temperatures. Furthermore, in arid environments where the soil surface is not significantly shaded by plant cover, direct solar heating may elevate deep soil temperature by 5 °C or more (Passey et al., 2010; Quade et al., 2011). Soil morphology in Axhandle Canyon is suggestive of significant aridity (Retallack, 2005), with background mean annual precipitation amounts of ~400 mm, suggesting soils may have been relatively bare of vegetative cover and subject to strong solar heating. Finally, the maximum burial depth of the North Horn and Flagstaff Formations in this area was only 1–2 km (Hintze, 1988). While Axhandle Canyon is today located on the margin of the Basin and Range province, a region with highly variable geothermal gradients (Blackett, 2004), the modern gradient for the locality is ~20 °C/km, so that maximum burial temperatures might have been as low as 40–60 °C. The potential therefore exists that unaltered nodule Δ_{47} measurements, reflecting early Paleogene summer soil temperatures, might be indistinguishable from samples altered by burial on the basis of temperature alone.

One potential criterion for evaluating the reliability of clumped isotope data is the plausibility of the calculated $\delta^{18}O_{H_2O}$ values having resulted from surface processes. Huntington et al. (2010) regarded lacustrine carbonates with temperatures and $\delta^{18}O_{H_2O}$ values higher than were considered plausible for regional lake waters as diagenetically altered. $\delta^{18}O_{H_2O}$ values calculated from our North Horn nodule samples span a range from −9‰ to −4‰ VSMOW (calculated using equations for dolomite, see Section 3.1). These values are significantly higher than the predicted value for modern meteoric precipitation at this locality of −13.9‰ (Bowen and Revenaugh, 2003), but given the major changes in topography and climate that have occurred since the early Paleogene, this is not surprising. Estimates of regional precipitation composition for the early Paleogene derived from carbonate oxygen isotopes range from −10‰ to −6‰ (Chamberlain et al., 2012), similar to our lowest $\delta^{18}O_{H_2O}$ estimates. Fricke (2003) determined the oxygen isotope composition of early Eocene river water, which should be broadly comparable to soil water, for several North American paleo-basins, utilizing $\delta^{18}O$ values of tooth enamel from the semi-aquatic mammal Coryphodon. Samples from the localities closest to the Axhandle basin, of Wasatchian age in the Green River Basin of Wyoming and the San Juan Basin of New Mexico, yielded average $\delta^{18}O_{river-water}$ values of −4.5‰ and −2.9‰, respectively. The high river water values were interpreted to reflect greater than modern rates of evaporation, a product of warm early Eocene temperatures. In comparison, our early Eocene samples provide an average

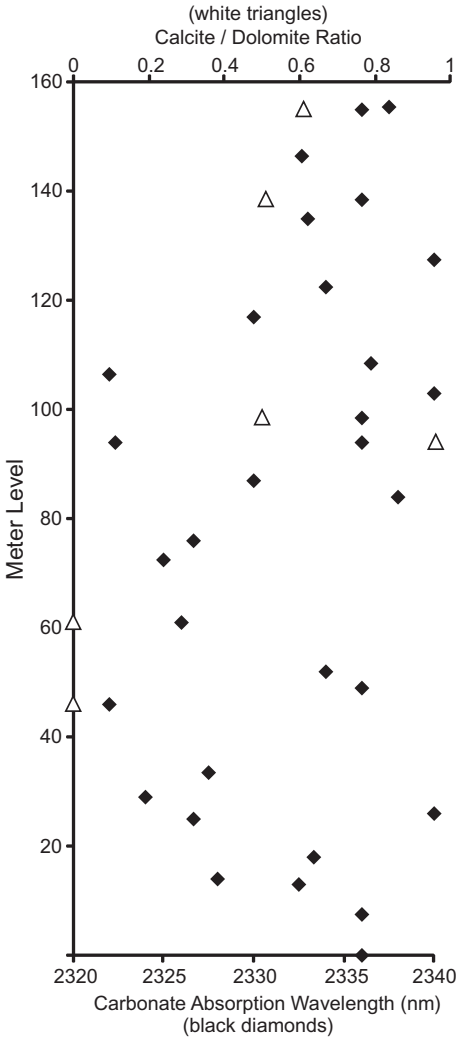

Fig. 6. IR spectroscopy and XRD mineral stratigraphy of Axhandle Canyon section. Black diamonds – wavelength of carbonate absorption feature, ~2320 = pure dolomite, ~2340 = pure calcite. White triangles – ratio of calcite to dolomite in samples analyzed with XRD.

$\delta^{18}O_{H_2O}$ value of $-6 \pm 2‰$. The Axhandle Basin's location, intermediate between the Green River and San Juan Basins along a north–south line and several hundred kilometers to the west, suggests good agreement with these values. Of note, $\delta^{18}O$ values for the Green River Basin were higher than those calculated for the Powder River and Big Horn Basins in northern Wyoming, which was suggested by Fricke (2003) to be a product of greater aridity in the Green River Basin. The carbonate nodules we sampled would have grow incrementally over intervals of hundreds to thousands of years each, and the large amount of carbonate analyzed for Δ_{47} should result in an integration of average conditions during the nodule's formation. Our samples show clear secular variation in their $\delta^{18}O_{H_2O}$ values, and we suggest that the most straightforward interpretation of these variations are relative changes in soil "dryness" that occurred during nodule formation.

Dennis and Schrag (2010) used carbonatites to assess the susceptibility of carbonate to diagenetic resetting of clumped isotope temperatures. As carbonatites are igneous carbonates which typically cool rapidly from melt, primary Δ_{47} and $\delta^{18}O_{CO_3}$ values should be highly distinct from those formed under surface conditions or plausible burial conditions. Carbonatites were identified as diagenetically altered when their $\delta^{18}O_{CO_3}$ and $\delta^{13}C$ values fell outside the range identified for igneous carbonates. In these carbonatites, a strong correlation ($R^2 = \sim 0.9$) exists between Δ_{47} and $\delta^{18}O_{CO_3}$, driven by the large differences in $\delta^{18}O_{CO_3}$ values between primary carbonatite and burial fluids. Our Δ_{47} and $\delta^{18}O_{CO_3}$ values do not suggest significant alteration utilizing these criteria, with minimal correlation ($r^2 = 0.05$), but the shift in temperature and $\delta^{18}O$ composition between paleosol formation and burial conditions will be much smaller than differences in the same factors for the altered carbonatites of that study, which may significantly weaken the correlation between Δ_{47} and $\delta^{18}O_{CO_3}$. Additionally, for this relationship to hold, water–rock ratios during diagenesis must be sufficiently high to facilitate significant oxygen exchange between the carbonate and aqueous phases. In the spatially and stratigraphically proximal Flagstaff Limestone, stratigraphic covariation in the $\delta^{13}C$ values of micrite and spar suggest water:rock ratios were relatively low (10–50), and in some instances similar covariation in $\delta^{18}O$ suggested ratios <1 (Banner and Hanson, 1990; Bowen et al., 2008).

Cross plots of $\delta^{13}C_{CO_3}$ vs. $\delta^{18}O_{CO_3}$ and Δ_{47}-derived temperatures vs. $\delta^{18}O_{H_2O}$ show some distinctions between the diagenetic categories (Fig. 7). When considered within the petrographic subsets, category 1 nodules show the strongest relationship between T and $\delta^{18}O_{H_2O}$. Category 2 nodules exhibit considerable variation in $\delta^{18}O_{H_2O}$ despite similar temperatures, while the category 3 nodules are the most uniform in both T and $\delta^{18}O_{H_2O}$. This may be a product of varying degrees of diagenetic overprinting affecting the T estimates from different categories of nodules. An alternate hypothesis is that the category 1 and 2 nodules are responding to changes in isotopic composition of meteoric precipitation, degree of soilwater evaporation, or seasonality of carbonate precipitation, independent of major temperature shifts (Section 4.4). Spar microsamples obtained from nodules exhibit significantly different $\delta^{18}O_{CO_3}$ values from the Flagstaff Fm. spar, and calculations of possible combinations of temperature and $\delta^{18}O_{H_2O}$ values in equilibrium with these microsamples show that the nodule spar could not have precipitated under the same conditions as the Flagstaff Fm. spar (Fig. 7B). In contrast, the nodule spars exhibit similar isotopic compositions to those of the associated micrite samples, and the range of equilibrium temperature and $\delta^{18}O_{H_2O}$ values for these samples intersects the population of values observed for the nodule micrites. The nodule micrite and spar are therefore likely to have formed in similar temperature and water composition conditions, suggesting two possible interpretations – that the micrite isotopic composition has been reset and records the same burial conditions as the spar, or that the spar formed early in the diagenetic process and records near-surface conditions similar to the micrite. The isotopic results alone do not present compelling evidence for either interpretation over the other.

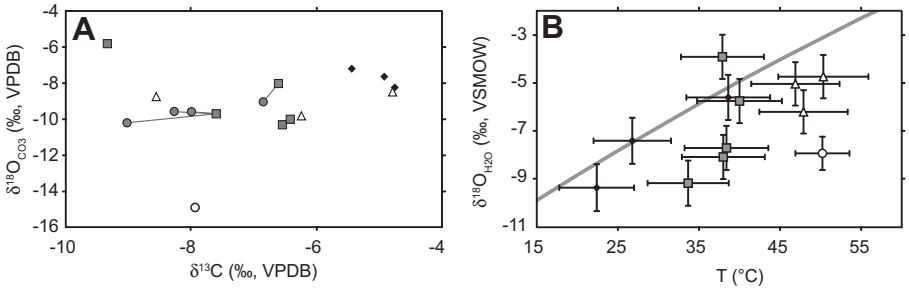

Fig. 7. Isotopic crossplots for all clumped isotope samples. (A) $\delta^{13}C_{CO_3}$ vs. $\delta^{18}O_{CO_3}$; (B) Δ_{47}-derived T vs. $\delta^{18}O_{H_2O}$, black diamonds – category 1 samples; gray squares – category 2; white triangles – category 3, white circle – Flagstaff Formation limestone spar sample, gray circles – North Horn Formation nodule spar microsamples. Gray lines in A tie spar microsamples to the nodule micrite from which they were obtained. Gray line in B represents T vs. $\delta^{18}O_{H_2O}$ curve for samples with $\delta^{18}O_{CO_3}$ composition equal to the average of values obtained from North Horn nodule spar microsamples. Error bars 1σ for estimation of temperature and $\delta^{18}O_{H_2O}$.

4.2. Combined isotopic and petrographic screening

The three categories of nodule samples have characteristics that indicate different potential extents of alteration during burial diagenesis, which may be associated with complete or partial resetting of their Δ_{47} values to reflect conditions in the subsurface. Single-factor ANOVA of Δ_{47} values identifies the three categories as distinct ($p = 0.004$), while t-tests indicate that category 3 is more distinct from categories 1 ($p = 0.03$) and 2 ($p = 0.0005$) than 1 and 2 are from each other ($p = 0.11$). This result, as well as the clustering of the samples in $\delta^{13}C_{CO_3}$ vs. $\delta^{18}O_{CO_3}$ and Δ_{47} vs. $\delta^{18}O_{H_2O}$ space (Fig. 7), further confirms our categorization of the samples based on their petrographic textures.

Category 1 samples have completely homogeneous micritic textures under both transmitted light and cathodoluminescence. If recrystallization has occurred in these samples, it either completely altered and re-homogenized the nodules or proceeded without introducing any heterogeneity detectible under transmitted, CL or electron microscopy. That these samples also exhibit the lowest formation temperatures further suggests that the homogeneity of their texture reflects an original, formation fabric. Category 1 nodules lack pores or large cracks through which burial fluids could have easily travelled, which may explain why they display the least evidence of diagenetic alteration. While the potential exists for solid-state resetting of Δ_{47} at temperatures >200 °C (Eiler et al., 2009), estimated burial depths (Hintze, 1988) and geothermal gradients (Blacket, 2004) and the relatively low temperatures indicated by the Δ_{47} results suggest it is unlikely that maximum burial temperatures reached this threshold.

Category 2 samples exhibit homogeneous micrite textures under both transmitted light and CL, but do contain variable amounts of pore-filling calcite cement which could have precipitated under burial conditions. Although care was taken to avoid taking spar-containing subsections of nodules for Δ_{47} measurement, the relatively large amounts of material required for these analyses increases the possibility that substantial spar was included. Spar from these nodules displays very similar luminescence behavior to the surrounding micrite, suggesting that at least the chemical conditions of precipitation were also similar. While we cannot distinguish early-burial, phreatic zone spar from deeper burial cements on the basis of texture alone, the absence of multiple identifiable generations of spar precipitation, or of zonation in the spar luminescence or EDX composition of category 2 samples, suggests that pore space in these nodules was filled in a single episode during their history. The presence of sparry calcite, if it precipitated near maximum burial depth, could shift measured Δ_{47} towards lower values through a mixing relationship. A weak relationship exists between % spar and Δ_{47} within the subset of category 1 and 2 samples, but is not significant at the 95% confidence interval ($r^2 = 0.41$, $p = 0.085$). Given that the spar does not exhibit a signficant $\delta^{18}O_{CO_3}$ offset relative to the coexisting micrite, and has very similar luminescence, we suggest that the most plausible interpretation is for the spar to have formed early in the diagenetic history of the nodules and at temperatures similar to those in which the surrounding micrite formed. If this is correct, it is unlikely that the amounts of spar present in the category 2 nodules have significantly altered their Δ_{47} values.

Category 3 samples exhibit extensive heterogeneity under both transmitted light and CL. Many areas in category 3 samples possess a granular texture under transmitted light (Fig. 4A) that is "speckled" under CL (Fig. 3C), suggesting extensive recrystallization of the micritic matrix. Category 3 nodules are also highly fractured on a microscopic scale, providing pathways for fluid flow that could promote alteration. Category 3 samples are similarly heterogenous under CL, suggesting that recrystallization may have occurred under very different redox conditions, consistent with burial diagenesis. Spar in the larger pores exhibits zonation of luminescence and texture, suggestive of multiple phases of spar precipitation under varying redox conditions, consistent with burial alteration. Precipitation temperatures obtained from category 3 samples are statistically distinct from the other samples, but given the maximum burial temperature of 40–60 °C inferred from both the Flagstaff Fm. spar sample and modern geothermal gradient, recrystallization would have to be nearly complete to produce these temperature values solely from burial recrystallization, a scenario which is not supported by the continued presence of microcrystalline dolomite in these samples. Category 3 $\delta^{18}O_{H_2O}$ values are not distinct from the other nodules,

which might suggest that their recrystallization occurred at low water/rock ratios.

4.3. Origin of dolomite

Petrographic and SEM analysis show that where dolomite occurs in nodules, it comprises the microcrystalline micrite of the nodule. Where present, spar crystals have distinct boundaries from the microcrystalline micrite (Figs. 3B and 5B). Textural relationships therefore demonstrate that spar represents a later phase of precipitation, filling originaly existing pore space. In all cases, petrography and EDX results indicate that this spar is calcite. Dolomitization as a result of burial diagenesis typically results in crystal coarsening (Driese et al., 1993) and chemical zonation detectable under CL (Solomon and Walkden, 1985), features which are not present in the nodule dolomicrite. It is possible that the dolomicrite is a very early, mimetic replacement of calcite, but in such cases an isopachous rim of acicular dolomite is typically present (Gómez-Gras and Alonso-Zarza, 2003), a trait missing from Axhandle nodules.

In modern systems, primary dolomite occurs far more commonly as a lacustrine precipitate (Last, 1990), rather than a pedogenic product. The Axhandle Canyon section was located on a floodplain marginal to paleo-Lake Flagstaff, which underwent multiple, repeated phases of dolomite precipitation (Stanley and Collinson, 1979; Bowen et al., 2008) and eventually expanded to cover the study section, as indicated by the deposition of lacustrine limestone and dolostone at the top of the section. However, several lines of evidence suggest that the nodular dolomite recovered from Axhandle Canyon is not lacustrine in origin. Paleosol horizons from which nodules were recovered commonly exhibit branching root traces and lack gleyed horizons, indicating the absence of waterlogged conditions. Further, isotope ratios for Flagstaff carbonates recovered from above the Axhandle Canyon section are distinct from nodular dolomite values, particularly for $\delta^{13}C$ (Fig. 8). While there is no evidence that the nodular dolomite has a lacustrine origin, the proximity of Lake Flagstaff likely played a crucial role in the mineralogy of soil carbonate. Dolomitic mudflats in the Flagstaff basin (Bowen et al., 2008) could have provided a source of magnesium, either as windblown dust or through periodic interaction of lake and soil waters during intermittent expansions of Lake Flagstaff, elevating soil Mg/Ca ratios to levels favorable for dolomite precipitation.

Dolomite formation is generally considered to require elevated Mg/Ca ratios and high carbonate ion concentrations. While SO_4^{2-} has a highly inhibitive effect on dolomite precipitation, Burton et al. (1992) suggested that highly elevated Mg/Ca ratios and high salinity can overcome this inhibitive effect and allow dolomite to precipitate. Pedogenic dolomite occurs in modern soils from Hawaii forming in basaltic parent material (Capo et al., 2000) that can supply additional magnesium for dolomite precipitation. However, the parent materials for North Horn paleosols are fluvial and alluvial silt, sand and mud derived from the advancing Sevier thrust front (Bowen and Bowen, 2008; Gierlowski-Kordesch et al., 2008), and do not contain unusually magnesium-rich material. If the necessary magnesium was instead supplied as windblown dust from Lake Flagstaff, dolomite precipitation would therefore be limited to the uppermost soil, as the additional magnesium would be quickly incorporated into soil carbonate. Pedogenic dolomite has also been found precipitating in modern saline soils from Alberta (Kohut et al., 1995), where high evaporation rates can produce pore waters with sufficiently high Mg/Ca ratios and carbonate ion concentrations to precipitate dolomite. The calcitic mineralogy of pore-filling spar in our sample set suggests evaporation rates may have played a critical role in regulating the micritic mineralogy. Once isolated from the surface, deeper groundwater would be less enriched in Mg^{2+} and CO_3^{2-}, causing the preferred carbonate mineralogy to shift from dolomite to calcite.

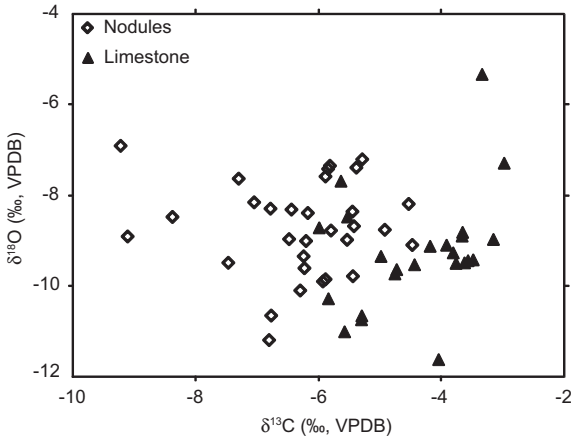

Fig. 8. $\delta^{13}C$ vs. $\delta^{18}O$ for paleosol nodules and lacustrine carbonates from the north wall of Axhandle Canyon. $\delta^{13}C$ values for the two substrates are statistically distinct ($p << 0.001$).

Our data therefore suggest that pedogenic dolomite in the upper North Horn Formation is a product of two factors, the proximity of a dolomite-precipitating lake basin, and hyperaridity associated with Paleocene–Eocene climate shifts. Windblown carbonate dust high in magnesium, combined with highly evaporative saline soil waters, would promote the precipitation of dolomite within the uppermost tens of centimeters of the soil horizon. As a soil was buried, these influences would wane, and carbonate formed in all subsequent diagenesis would occur as calcite.

4.4. Reconstructed Paleocene–Eocene temperatures and $\delta^{18}O_{H_2O}$

Our assessment suggests that the Δ_{47}-reconsctructed temperature and water oxygen isotope ratios for category 3 nodules are not likely to faithfully record early Paleogene surface conditions. Although it is impossible to constrain exactly when in their burial history these nodules were partially recrystallized, the relatively small offset of their Δ_{47} values from the other samples lends weight to our interpretation that maximum burial temperatures did not exceed 100 °C. Nonetheless, partial alteration and the presence of significant amounts of chemically distinct spar in these nodules suggest that their clumped isotope geochemistry likely averages information on surface and sub-surface conditions.

The average late Paleocene (pre-carbon isotope excursion) temperature obtained from category 1 and 2 samples at Axhandle Canyon is 35 °C, although the Paleocene data are highly variable. Values for the early Eocene (CIE and post-CIE) are slightly warmer (39 °C). Comparable estimates from other proxies are not available in central Utah. Paleofloral studies for the early Eocene of southwestern Wyoming (Wilf, 2000), where regional climate models predict Eocene temperatures ~2 °C lower than in central Utah (Sewall and Sloan, 2006), give mean annual temperature estimates of ~20 °C. Although our coolest clumped isotope temperature approaches this value, this sample is located ~34 meters below the PETM CIE. Based on long-term sediment accumulation rates of 31–75 m/Myr (Bowen and Bowen, 2008) derived from the magnetostratigraphy of Talling et al. (1994), this sample reflects late Paleocene conditions, predating the P/E boundary by 0.4–1.0 Myr. All of our Eocene temperature estimates are significantly warmer than the floral assemblage estimates. These paleofloral temperatures were derived from leaf-margin analysis (LMA), a univariate approach that assumes a linear relationship between mean annual temperature and the proportion of toothed leaves within a particular floral assemblage (Wolfe, 1979; Wing and Greenwood, 1993). Recent work (Little et al., 2010) has suggested that the proportion of toothed-leaf species within a population has a significant phylogenetic component. More recently developed multivariate approaches to paleofloral temperature reconstructions (Peppe et al., 2011) have produced warmer MAT estimates that agree more closely with other paleoclimate proxies. As we suggest, clumped-isotope temperature estimates from paleosol carbonate likely reflect warm season soil temperatures rather than mean annual air temperatures, and in arid environments potentially have a further warm bias introduced by strong solar heating of bare soils. Temporal changes in plant cover, and thus in direct soil heating could therefore also exaggerate the response to air temperature changes. When the potential biases of these two methods are considered, their temperature estimates might be considerably closer than is first apparent, and both together can provide complimentary insights into ancient climates.

Our stratigraphic record contains two prominent temperature maxima, the largest associated with the PETM CIE at 60 m and the other, slightly smaller excursion occuring ~40 m below it (Fig. 1). This excursion is identified from two samples of categories 1 and 3. The Axhandle section might therefore record a major temperature excursion prior to the PETM. Sedimentation rates indicate this event preceded the PETM by some 0.5–1.2 million years. Although this broad range of age estimates precludes precise interpretaion of the record, some evidence for pre-PETM warming events has been observed at other sites. A record of $\delta^{18}O$ in mammalian tooth enamel from the Bighorn Basin (Secord et al., 2010) exhibits a ~1.5‰ positive excursion at 57 Ma. In the Mead Stream, New Zealand section of Hollis et al. (2005), hyperthermals (e.g. PETM, ETM-1 & 2) are correlated with marl layers interpreted to represent enhanced terrigenous input. Several of these marls occur below the PETM interval, with the best correlation to our temperature event being "Mudstone C", 20 m below the PETM. The lower Axhandle temperature maximum does not coincide with any major changes in bulk isotope ($\delta^{13}C$, $\delta^{18}O$) composition, increasing the potential that this excursion, if it represents a climatic event, might have gone unidentified in many previous studies.

The 38 °C temperature recorded by sample NH060122, at 55.5 m is particularly intriguing, as it comes from the portion of the record where the lowest $\delta^{13}C$ values are recorded, but does not exhibit temperatures distinct from those of post-PETM nodules. This sample does display very high $\delta^{18}O_{H_2O}$, suggesting a significant difference in hydroclimatologic conditions. We suggest that one possible explanation for these observations might involve changes in the seasonality of carbonate nodule precipitation, which tends to coincide with seasonal periods of drying in the soil (Breecker et al., 2009; Passey et al., 2010). If the Axhandle Basin site experienced a significant increase in aridity during the PETM, as previously suggested (Bowen and Bowen, 2008) and as consistent with the large increase in reconstructed $\delta^{18}O_w$ values for PETM samples in our study, this may have shifted seasonal soil dessication and the period of carbonate formation to occur during an earlier, cooler part of the year. An alternative hypothesis, not mutually exclusive, is that this sample, and potentially others, underwent some amount of recrystallization during very early burial, under near-closed system conditions. Temperatures recorded by Δ_{47} would thus be partially reset to those of the overlying soil at time of recrystallization, while the original bulk isotope ($\delta^{13}C$, $\delta^{18}O$) compositions may have been retained.

5. CONCLUSIONS

We have used a combination of isotopic and petrographic techniques to evaluate the presence and origin of pedogenic dolomite in paleosols spanning the Paleocene–Eocene boundary in central Utah, and developed a paleoclimate record from this section utilizing clumped isotope thermometry. The existence of pedogenic dolomite in the Axhandle Canyon section is the result of a unique combination of climate and geochemical conditions, including very warm regional climate conditions and the proximity of the dolomite-precipitating Lake Flagstaff. While the presence of micritic and sparry calcite formed during burial complicates interpretation of some samples, petrographic, mineralogical, and chemical data allow for the identification of samples which have experienced major diagenetic alteration and support a hypothesis that the majority of samples still retain an original signal of surface conditions. Our work has allowed us to obtain temperature values which are likley to reflect warm-season soil temperatures for the study area during the late Paleocene and early Eocene. Finally, we suggest that given the high degree of heterogeneity observed within our sample set, future studies should undertake thorough petrographic analysis of potential samples prior to final sample selection, in order to identify those samples most likely to retain a primary signal.

ACKNOWLEDGMENTS

The authors were assisted by K. Nielson and L. Tapanila in the field, and by G. Henkes, M. Suarez, S. Story and Xuanhao Sun in

the lab. We would like to thank K. Huntington and two anonymous reviewers for their feedback. Support for this work was provided by US National Science Foundation Grants EAR-0628302 and OCE-0902882 to G.J.B.

APPENDIX A. SUPPLEMENTARY DATA

Supplementary data associated with this article can be found, in the online version, at http://dx.doi.org/10.1016/j.gca.2013.02.005.

REFERENCES

Affek H. and Eiler J. M. (2006) Abundance of mass 47 CO_2 in urban air, car exhaust, and human breath. *Geochim. Cosmochim. Acta* **70**, 1–12.

Banner J. L. and Hanson G. N. (1990) Calculation of simultaneous isotopic and trace element variations during water–rock interaction with applications to carbonate diagenesis. *Geochim. Cosmochim. Acta* **54**, 3123–3137.

Bijl P. K., Schouten S., Sluijs A., Reichart G. J., Zachos J. C. and Brinkhuis H. (2009) Early Palaeogene temperature evolution of the southwest Pacific Ocean. *Nature* **461**, 776–779.

Blackett R. E. (2004) *Geothermal Gradient Data for Utah*. Utah Geological Survey, Salt Lake City, UT.

Bowen G. J. and Bowen B. B. (2008) Mechanisms of PETM global change constrained by a new record from central Utah. *Geology* **36**, 379–382.

Bowen G. J. and Revenaugh J. (2003) Interpolating the isotopic composition of modern meteoric precipitation. *Water Resour. Res.* **39**, 1299.

Bowen G. J., Beerling D. J., Koch P. L., Zachos J. C. and Quattlebaum T. (2004) A humid climate state during the Paleocene/Eocene thermal maximum. *Nature* **432**, 495–499.

Bowen G. J., Daniels A. L. and Bowen B. B. (2008) Paleoenvironmental isotope geochemistry and paragenesis of lacustrine and palustrine carbonates, Flagstaff Formation, central Utah, U.S.A. *J. Sediment. Res.* **78**, 162–174.

Breecker D. O., Sharp Z. D. and McFadden L. D. (2009) Seasonal bias in the formation and stable isotopic composition of pedogenic carbonate in modern soils from central New Mexico, USA. *Geol. Soc. Am. Bull.* **121**, 630–640.

Burton E. A., Hahn T. and Machel T. H. (1992) Magnesium sulfate brine lakes that precipitate dolomite: evidence that Mg^{2+} dehydration is more important than removal of SO_4^{2-} inhibition in dolomite formation. In *Water–rock interaction* (eds. Y. K. Kharaka and A. S. Maest). Balkema, Rotterdam, the Netherlands.

Capo R. C., Whipkey C. E., Blachère J. R. and Chadwick O. A. (2000) Pedogenic origin of dolomite in a basaltic weathering profile, Kohala peninsula, Hawaii. *Geology* **28**, 271–274.

Chamberlain C. P., Mix H. T., Mulch A., Hren M. T., Kent-Corson M. T., Davis S. J., Horton T. W. and Graham S. A. (2012) The Cenozoic climatic and topographic evolution of the western North American Cordillera. *Am. J. Sci.* **312**(2), 213–262.

Dennis K. J. and Schrag D. P. (2010) Clumped isotope thermometry of carbonatites as an indicator of diagenetic alteration. *Geochim. Cosmochim. Acta* **74**, 4110–4122.

Dennis K. J., Affek H. P., Passey B. H., Schrag D. P. and Eiler J. M. (2011) Defining an absolute reference frame for 'clumped' isotope studies of CO_2. *Geochim. Cosmochim. Acta* **75**, 7117–7131.

Diefendorf A. F., Mueller K. E., Wing S. L., Koch P. L. and Freeman K. H. (2010) Global patterns in leaf ^{13}C discrimination and implications for studies of past and future climate. *Proc. Natl. Acad. Sci. USA* **107**, 5738–5743.

Driese, S.G., Mora, C.I., And Cotter, E. (1993) Buffalo Mountain paleosol, Duncannon Member of Catskill Formation (Upper Devonian) near Newport, PA, in Driese, S.G., Paleosols, Paleoclimate, and Paleoatmospheric CO2; Paleozoic Paleosols of Central Pennsylvania. University of Tennessee, Department of Geological Sciences, Studies in Geology 22, 50–66.

Eagle R. A., Tütken T., Martin T. S., Tripati A. K., Fricke H. C., Connely M., Cifelli R. L. and Eiler J. M. (2011) Dinosaur body temperatures determined from isotopic (^{13}C–^{18}O) ordering in fossil biominerals. *Science* **333**, 443–445.

Eiler J. M., Bonifacie M. and Daeron M. (2009) 'Clumped Isotope' thermometry for high-temperature problems. *Geochim. Cosmochim. Acta* **73**, A322.

Ferry J. M., Passey B. H., Vasconcelos C. and Eiler J. M. (2011) Formation of dolomite at 40–80 °C in the Latemar carbonate buildup, Dolomites, Italy, from clumped isotope thermometry. *Geology* **39**, 571–574.

Fricke H. C. (2003) Investigation of early Eocene water-vapor transport and paleoelevation using oxygen isotope data from geographically widespread mammal remains. *Geol. Soc. Am. Bull.* **115**, 1088–1096.

Gaffey S. J. (1986) Spectral reflectance of carbonate minerals in the visible and near-infrared (0.35-2.55 microns): calcite, aragonite, and dolomite. *Am. Mineral.* **71**, 151–162.

Ghosh P., Adkins J., Affek H., Balta B., Guo W., Schauble E. A., Schrag D. P. and Eiler J. M. (2006) ^{13}C–^{18}O bonds in carbonate minerals: a new kind of paleothermometer. *Geochim. Cosmochim. Acta* **70**, 1439–1456.

Gierlowski-Kordesch E. H., Jacobson A. D., Blum J. D. and Garces B. L. V. (2008) Watershed reconstruction of a Paleocene–Eocene lake basin using Sr isotopes in carbonate rocks. *Geol. Soc. Am. Bull.* **120**, 85–95.

Gómez-Gras D. and Alonso-Zarza A. M. (2003) Reworked calcretes: their significance in the reconstruction of alluvial sequences (Permian and Triassic, Minorca, Balearic Islands, Spain). *Sediment. Geol.* **158**, 299–319.

Guo W., Mosenfelder J. L., Goddard W. A. and Eiler J. M. (2009) Isotopic fractionations associated with phosphoric acid digestion of carbonate minerals: insights from first principles theoretical modeling and clumped isotope measurements. *Geochim. Cosmochim. Acta* **73**, 7203–7225.

He T., Chen Y., Balsam W., Sheng X., Liu L., Chen J. and Ji J. (2012) Distribution and origin of protodolomite from the late Miocene–Pliocene red clay formation, Chinese Loess Plateau. *Geochem. Geophys. Geosyst.* **13**, Q06004.

Hemming N. G., Meyers W. J. and Grams J. C. (1989) Cathodoluminescence in diagenetic calcites: the role of Fe and Mn as deduced from electron probe and spectrophotometric measurements. *J. Sediment. Petrol.* **59**, 404–411.

Hintze, L.F. (1988) Geological History of Utah. Brigham Young University, Provo, Utah, Geology Studies, Special Publication 7, 202 pp.

Hollis C. J., Dickens G. R., Field B. D., Jones C. M. and Strong C. P. (2005) The Paleocene–Eocene transition at Mead Stream, New Zealand: a southern Pacific record of early Cenozoic global change. *Palaeogeogr. Palaeoclimatol. Palaeoecol.* **215**, 313–343.

Huber M. and Caballero R. (2011) The early Eocene equable climate problem revisited. *Clim. Past* **7**, 241–304.

Huntington K. W., Eiler J. M., Affek H. P., Guo W., Bonifacie M., Yeung L. Y., Thiagarajan N., Passey B., Tripati A., Daëron M. and Came R. (2009) Methods and limitations of 'clumped' CO_2 isotope (Δ_{47}) analysis by gas-source isotope ratio mass spectrometry. *J. Mass Spectrom.* **44**, 1318–1329.

Huntington K. W., Wernicke B. P. and Eiler J. M. (2010) Influence of climate change and uplift on Colorado Plateau paleotemperatures from carbonate clumped isotope thermometry. *Tectonics* **29**, TC3005.

Huntington K. W., Budd D. A., Wernicke B. P. and Eiler J. M. (2011) Use of clumped-isotope thermometry to constrain the crystallization temperature of diagenetic calcite. *J. Sediment. Res.* **81**, 656–669.

Kearsey T., Twitchett R. J. and Newell A. J. (2012) The origin and significance of pedogenic dolomite from the Upper Permian of the South Urals of Russia. *Geol. Mag.* **149**, 291–307.

Keating-Bitonti C. R., Ivany L. C., Affek H. P., Douglas P. and Samson S. D. (2011) Warm, not super-hot, temperatures in the early Eocene subtropics. *Geology* **39**, 771–774.

Kessler J. L. P., Soreghan G. S. and Wacker H. J. (2001) Equatorial aridity in western Pangea: lower Permian loessite and dolomitic paleosols in northeastern New Mexico, U.S.A. *J. Sediment. Res.* **71**, 817–832.

Kim S. and O'Neil J. R. (1997) Equilibrium and nonequilibrium oxygen isotope effects in synthetic carbonates. *Geochim. Cosmochim. Acta* **61**, 3461–3475.

Kohut C., Muehlenbachs K. and Dudas M. J. (1995) Authigenic dolomite in a saline soil in Alberta, Canada. *Soil Sci. Soc. Am. J.* **59**, 1499–1504.

Last W. M. (1990) Lacustrine dolomite – an overview of modern, Holocene, and Pleistocene occurrences. *Earth Sci. Rev.* **27**, 221–263.

Lawton T. F. and Trexler J. H. (1991) Piggyback basin in the Sevier orogenic belt, Utah: implications for development of the thrust wedge. *Geology* **19**, 827–830.

Little S. A., Kembel S. W. and Wilf P. (2010) Paleotemperature proxies from leaf fossils reinterpreted in light of evolutionary history. *PLoS One* **5**(12).

Machel., H.G., and Burton, E.A. (1991) Factors governing cathodoluminescence in calcite and dolomite, and their implications for studies of carbonate diagenesis, in Barker, C.E. and Kopp, O.C., editors, Luminescence microscopy and spectroscopy: qualitative and quantitative applications. Soc. for Sediment. Geol., 37–57.

McInerney F. A. and Wing S. L. (2011) The Paleocene–Eocene Thermal Maximum: a perturbation of carbon cycle, climate and biosphere with implications for the future. *Annu. Rev. Earth Planet. Sci.* **39**, 489–516.

Passey B. H., Levin N. E., Cerling T. E., Brown F. H. and Eiler J. M. (2010) High-temperature environments of human evolution in East Africa based on bond ordering in paleosol carbonates. *Proc. Natl. Acad. Sci.* **107**, 11245–11249.

Peppe D. J., Royer D. L., Cariglino B., Oliver S. Y., Newman S., Leight E., Enikolopov G., Fernandez-Burgos M., Herrera F., Adams J. M., Correa E., Currano E. D., Erickson J. M., Hinojosa L. F., Hoganson J. W., Iglesias A., Jaramillo C. A., Johnson K. R., Jordan G. J., Kraft N. J. B., Lovelock E. C., Lusk C. H., Niinemets U., Peñuelas J., Rapson G., Wing S. L. and Wright I. J. (2011) Sensitivity of leaf size and shape to climate: global patterns and paloclimatic applications. *New Phytol.* **190**, 724–739.

Quade J., Breecker D. O., Daëron M. and Eiler J. (2011) The paleoaltimetry of Tibet: an isotopic perspective. *Am. J. Sci.* **311**, 77–115.

Retallack G. J. (2005) Pedogenic carbonate proxies for amount and seasonality of precipitation in paleosols. *Geology* **33**, 333–336.

Rich R. H. V. and Collinson J. W. (1973) First mammalian fossil from Flagstaff limestone, Central Utah – Vulpavus Australis (Carnivora-Miacidae). *J. Paleontol.* **47**, 854–860.

Schauble E. A., Ghosh P. and Eiler J. M. (2006) Preferential formation of ^{13}C–^{18}O bonds in carbonate minerals, estimated using first-principles lattice dynamics. *Geochim. Cosmochim. Acta* **70**, 2510–2529.

Schouten S., Woltering M., Rijpstra W. I. C., Sluijs A., Brinkhuis H. and Damsté J. S. S. (2007) The Paleocene–Eocene carbon isotope excursion in higher plant organic matter: differential fractionation of angiosperms and conifers in the Arctic. *Earth Planet. Sci. Lett.* **258**, 581–592.

Secord R., Gingerich P. D., Lohmann K. C. and MacLeod K. G. (2010) Continental warming preceding the Paleocene–Eocene thermal maximum. *Nature* **467**, 955–958.

Sewall J. O. S. and Sloan L. C. (2006) Come a little bit closer: a high-resolution climate study of the early Paleogene Laramide foreland. *Geology* **34**, 81–84.

Sheldon N. D. and Tabor N. J. (2009) Quantitative paleoenvironmental and paleoclimatic reconstruction using paleosols. *Earth-Sci. Rev.* **95**, 1–52.

Sloan L. C. (1994) Equable climates during the early Eocene: significance of regional paleogeography for North American climate. *Geology* **22**, 881–884.

Smith F. A., Wing S. L. and Freeman K. H. (2007) Magnitude of the carbon isotope excursion at the Paleocene–Eocene thermal maximum: the role of plant community change. *Earth Planet. Sci. Lett.* **262**, 50–65.

Solomon S. T. and Walkden G. M. (1985) The application of cathodoluminescence to interpreting the diagenesis of an ancient calcrete profile. *Sedimentology* **32**, 877–896.

Stanley K. O. and Collinson J. W. (1979) Depositional history of Paleocene–lower Eocene Flagstaff Limestone and coeval rocks, central Utah. *Am. Assoc. Petrol. Geol. Bull.* **63**, 311–323.

Talling P. J., Burbank D. W., Lawton T. F., Hobbs R. S. and Lund S. P. (1994) Magnetostratigraphic chronology of Cretaceous-to-Eocene thrust belt evolution, central Utah, USA. *J. Geol.* **102**, 181–196.

Vasconcelos C., McKenzie J. A., Warthmann R. and Bernasconi S. M. (2005) Calibration of the $\delta^{18}O$ paleothermometer for dolomite precipitated in microbial cultures and natural environments. *Geology* **33**, 317–320.

Wang Z., Schauble E. A. and Eiler J. M. (2004) Equilibrium thermodynamics of multiply substituted isotopologues of molecular gases. *Geochim. Cosmochim. Acta* **68**, 4779–4797.

Wilf P. (2000) Late Paleocene–early Eocene climate changes in southwestern Wyoming: Paleobotanical analysis. *Geol. Soc. Am. Bull.* **112**, 292–307.

Wing S. L. and Greenwood D. R. (1993) Fossils and fossil climate: the case for equable continental interiors in the Eocene. *Philos. Trans. R. Soc. London* **341**, 243–252.

Wolfe, J. A. (1979) Temperature parameters of humid to mesic forests of eastern Asia and relation to forests of other regions in the Northern Hemisphere and Australasia. U.S. Geol. Survey Professional Paper 1106.

Zachos J. C., Pagani M., Sloan L., Thomas E. and Billups K. (2001) Trends, rhythms, and aberrations in global climate 65 Ma to present. *Science* **292**, 686–693.

Zachos J. C., Schouten S., Bohaty S. M., Quattlebaum T., Sluijs A., Brinkhuis H., Gibbs S. J. and Bralower T. J. (2006) Extreme warming of mid-latitude coastal ocean during the Paleocene Eocene Thermal Maximum: inferences from TEX86 and isotope data. *Geology* **34**, 737–740.

Associate editor: Brian W. Stewart